Redox Biology 85 (2025) 103758

Contents lists available at ScienceDirect

Redox Biology

journal homepage: www.elsevier.com/locate/redox

POLR1A inhibits ferroptosis by regulating TFAM-mediated mitophagy and iron homeostasis

Tuo Zhang [a,b,1], Yanyun Gao [a,b,c,1], Marcell Harhai [d], Alexis A. Jourdain [d], Thomas M. Marti [a,b], Erik Vassella [e], Zhang Yang [a,b,f,g,**], Qinghua Zhou [c,***], Patrick Dorn [a,b,****], Ren-Wang Peng [a,b,*]

[a] Department of General Thoracic Surgery, Bern University Hospital, Bern, Switzerland
[b] Department for BioMedical Research (DBMR), University of Bern, Bern, Switzerland
[c] Lung Cancer Institute/Lung Cancer Center, West China Hospital, Sichuan University, Chengdu, China
[d] Department of Immunobiology, University of Lausanne, CH-1066 Epalinges, Switzerland
[e] Institute of Tissue Medicine and Pathology, University of Bern, Bern, Switzerland
[f] Department of Thoracic Surgery, Fujian Medical University Union Hospital, Fuzhou, China
[g] Clinical Research Center for Thoracic Tumors of Fujian Province, Fuzhou, China

ARTICLE INFO

Keywords:
Ferroptosis
Iron metabolism
mitophagy
POLR1A
ATF4
TFAM

ABSTRACT

Evasion of programmed cell death (PCD) is a hallmark of cancer, yet the mechanisms underlying resistance to ferroptosis – an iron-dependent form of PCD triggered by excessive lipid peroxidation – remain incompletely understood. Here, we identify a previously unrecognized nucleolar-mitochondrial signaling axis that promotes ferroptosis resistance in pleural mesothelioma (PM) and potentially other cancers. This pathway involves RNA polymerase I (*PolI*) catalytic subunit A (POLR1A) and mitochondrial transcription factor A (TFAM), which together regulate mitophagy and intracellular iron metabolism to suppress ferroptosis. Mechanistically, POLR1A controls TFAM expression via the transcription factor ATF4, and this POLR1A-ATF4-TFAM axis inhibits mitophagy and limit mitophagy-dependent labile Fe^{2+} release, thereby preventing Fe^{2+}-driven lipid peroxidation. Disruption of this pathway through POLR1A or TFAM inhibition leads to Fe^{2+} accumulation and increased sensitivity to ferroptosis inducers (FINs). Notably, CX-5461, a first-in-class RNA *PolI* inhibitor currently in clinical trials, synergizes with GPX4 blockade to induce ferroptotic cell death both in vitro and in vivo. This therapeutic synergy extends beyond PM, suggesting broader relevance in ferroptosis-resistant cancers. Together, our findings reveal a novel mechanism of ferroptosis evasion and establish a promising combinatorial strategy to overcome therapy resistance in cancer.

1. Introduction

Pleural mesothelioma (PM) is a highly aggressive malignancy arising from the mesothelial lining of the thoracic cavity and lungs [1]. Its long latency – often exceeding 40 years – contributes to a growing global disease burden. Early-stage PM is typically asymptomatic, resulting in delayed diagnoses and poor clinical outcomes, with a median survival of approximately 15 months following chemotherapy. Unlike many other cancers, PM rarely habors common oncogenic mutations, limiting the efficacy of targeted therapies [2,3] and underscoring the urgent need for novel treatment strategies [4,5].

Ferroptosis, an iron-dependent form of programmed cell death characterized by the accumulation of lipid peroxides [6], has emerged as a potential therapeutic vulnerability in various cancers [7]. Initiated by ferrous iron (Fe^{2+})-driven Fenton chemistry, this process leads to oxidative membrane damage and cell death. Ferroptosis susceptibility is

* Corresponding author. Department of General Thoracic Surgery, Bern University Hospital, Bern, Switzerland.
** Corresponding author. Department of General Thoracic Surgery, Bern University Hospital, Bern, Switzerland.
*** Corresponding author. Lung Cancer Institute/Lung Cancer Center, West China Hospital, Sichuan University, Chengdu, China.
**** Corresponding author. Department of General Thoracic Surgery, Bern University Hospital, Bern, Switzerland.
E-mail address: renwang.peng@insel.ch (R.-W. Peng).
[1] Equal contribution to this work.

https://doi.org/10.1016/j.redox.2025.103758
Received 11 June 2025; Accepted 7 July 2025
Available online 8 July 2025

governed by the balance between iron metabolism and antioxidant defenses [8]. Two key regulators, SLC7A11 and glutathione peroxidase 4 (GPX4), form the core of the ferroptosis resistance machinery. SLC7A11 supports glutathione (GSH) synthesis by importing cystine, while GPX4 uses GSH to detoxify lipid hydroperoxides. Inhibitors such as erastin (SLC7A11), RSL3 and ML162 (GPX4) disrupt this protective axis, thereby triggering ferroptosis [6,8]. Dysregulation of iron homeostasis and redox metabolism, common features in cancer, can significantly alter ferroptosis sensitivity and are now recognized as actionable therapeutic targets [7].

Mitochondria play a central role in ferroptosis regulation through their functions in energy production, redox homeostasis, and iron metabolism [9]. One key mechanism in mitochondrial quality control is mitophagy, a selective autophagic process that removes damaged mitochondria to prevent excessive reactive oxygen species (ROS) production [10]. Under physiological conditions, mitophagy is protective, but when overactivated, it can release mitochondrial Fe^{2+} into the cytoplasm, fueling ROS accumulation and lipid peroxidation, thereby sensitizing cells to ferroptosis [11,12]. These findings highlight mitophagy as a context-dependent modulator of ferroptosis, bridging mitochondrial dynamics and iron metabolism.

Mitochondrial transcription factor A (TFAM) is critical for maintaining mitochondrial DNA (mtDNA) integrity and supporting oxidative phosphorylation (OXPHOS) [13]. Loss of TFAM disrupts mitochondrial function and activates mitophagy, linking mitochondrial fitness directly to ferroptosis sensitivity. The expression of TFAM and other mitochondrial homeostasis genes is regulated by the transcription factor ATF4, a central mediator of cellular stress responses [14]. Activated by nutrient deprivation, oxidative stress, and ER stress, ATF4 coordinates adaptive programs encompassing both the mitochondrial and ER stress responses. Through these pathways, ATF4 promotes mitochondrial biogenesis, maintains redox balance, and modulates mitophagy [14].

ATF4 also regulates biosynthetic activity during cellular stress. For example, under ER stress, cells suppress global protein synthesis to relieve the folding workload and conserve energy. As part of this response, ATF4 downregulates ribosome biogenesis (RiBi), an energetically demanding process required for cell growth and proliferation [15]. RiBi begins in the nucleolus, where RNA Polymerase I (*Pol*I) transcribes the 47S precursor ribosomal RNA (rRNA). Its catalytic subunit, POLR1A, is often overexpressed in cancer cells to support increased ribosome production [16–18]. These observations link ATF4 to nucleolar activity and downstream mitochondrial functions, although the underlying mechanisms remain largely undefined.

Given its central role in RiBi, POLR1A is an attractive therapeutic target in cancer [18]. CX-5461, a selective *Pol*I inhibitor now in clinical trials, blocks rRNA transcription, disrupts nucleolar integrity, and induces cancer cell death— especially in tumors with DNA repair defects [19–21]. Although CX-5461's effects on ribosome biogenesis is well established, its effects on mitochondrial regulation, mitophagy, and ferroptosis remain unexplored.

In this study, we uncover a previously unrecognized regulatory axis linking POLR1A, ATF4, and TFAM to mitophagy and ferroptosis in pleural mesothelioma. We show that POLR1A promotes TFAM expression through ATF4 and that inhibition of POLR1A activates mitophagy, increases cytosolic Fe^{2+} levels, and sensitizes PM cells to ferroptosis inducers. Furthermore, pharmacological inhibition of POLR1A with CX-5461 synergizes with GPX4 blockade to promote ferroptotic cell death and suppress tumor growth in vitro and in vivo. These findings reveal a novel mechanistic link between ribosome biogenesis and ferroptosis resistance and provide a promising therapeutic approach for targeting ferroptosis-evading cancers.

2. Methods and materials

2.1. Cell culture

Cancer cell lines (MESO-1, H2452, BE1143T, H1080T, DLD1) were previously described [22–24]. BE1143T is derived from a PM patient. All cells were authenticated by short tandem repeat (STR) profiling and regularly tested to ensure they were free of mycoplasma (Microsynth). RSL3 (CS-5650), ML162 (CS-0017910), doxycycline (Dox; CS-0009105), ferrostatin-1 (CS-0019733), deferoxamine (CS-0013559), liproxstatin-1 (CS-3994), CX-5461 (CS-0045136) and Quarfloxin (CS-0003553) were obtained from ChemScene.

2.2. Antibodies and beads

The following antibodies were used: POLR1A (Proteintech, #20595-1-AP); β-actin (Cell Signaling Technology/CST, #3700S); TFAM (Proteintech, #22586-1-AP); PERK (CST, #3192S); p-PERK (CST, #3179S); ATF4 (CST, #11815S); eIF2α (CST, #9722S); *p*-eIF2α (CST, #3398S); PARK2 (Proteintech, #14060-1-AP); GPX4 (abcam, Cat# ab125066); TP53(CST, Cat#9282S); SLC7A11(Proteintech, #26864-1-AP); CYTB (Proteintech, #55090-1-AP); ATP6(Proteintech, #55313-1-AP); TOMM20(CST, #42406S); Phospho-Histone H2A.X (Ser139) (CST, Cat#9718S); FTL(proteintech,10727-1-AP); NCOA4(NBP3-18136); LC3A/B(CST, #4108S), IRDye 680RD-conjugated donkey anti-mouse IgG (Lot #D20503-05) and IRDye 800CW-conjugated donkey anti-rabbit IgG (Lot #D01216-10) from Li-COR Biosciences. Signals from membrane-bound secondary antibodies were visualized using the Odyssey Infrared Imaging System (Li-COR Biosciences).

2.3. siRNA, shRNA and sgRNA

The siRNAs for PARK2 and ATF4 (SR321228; SR319410; Origene) were transfected using DMH13 (gift from Chem Bern). The shRNA sequences are as follows: POLR1A: 5′-GACGAGATGAATGCCCATTTC-3′ (#1); 5′-TACATCAACACCAACGAAATT-3′ (#2). TFAM: 5′-CGTGAGTATATTGATCCAGAA-3′ (#1); 5′-GTAAGTTCTTACCTTCGATTT-3′ (#2). GPX4: 5′-GTGGATGAAGATCCAACCCAA-3′ (#1); 5′-GCACATGGTTAACCTGGACAA-3(#2). The DNA oligos were annealed and ligated into the plko.1-tet-on plasmids (Addgene #21915). Retroviruses carrying the shRNA constructs were produced in 293T cells and used to infect target cells.

2.4. Overexpression plasmids

Human overexpression plasmids for ATF4 (Addgene #115969) and TFAM (pLV [Exp]-Bsd-CMV > hTFAM [NM_003201.3]) were obtained from Addgene and VectorBuilder, separately. The control empty vector (Addgene #125238) was got from Addgene. Lentiviruses carrying these overexpression plasmids were produced in 293T cells and used to infect target cells.

2.5. Cell death assay

Cells were seeded into 6-well plates at a density of 50 % confluence. The following day, the cells were treated with various drugs for the appropriate amount of time. To measure cell death, cells were digested, collected, and then assessed using trypan blue dye (Thermo Scientific, 15250061) in conjunction with cell counting.

2.6. Cell viability assay and clonogenic survival assay

Cell viability was measured using the acid phosphatase (APH) assay as previously described [22]. Each data point represents the average of triplicate measurements from three independent experiments (n = 3). Bliss scores and their contour heatmaps were generated using the

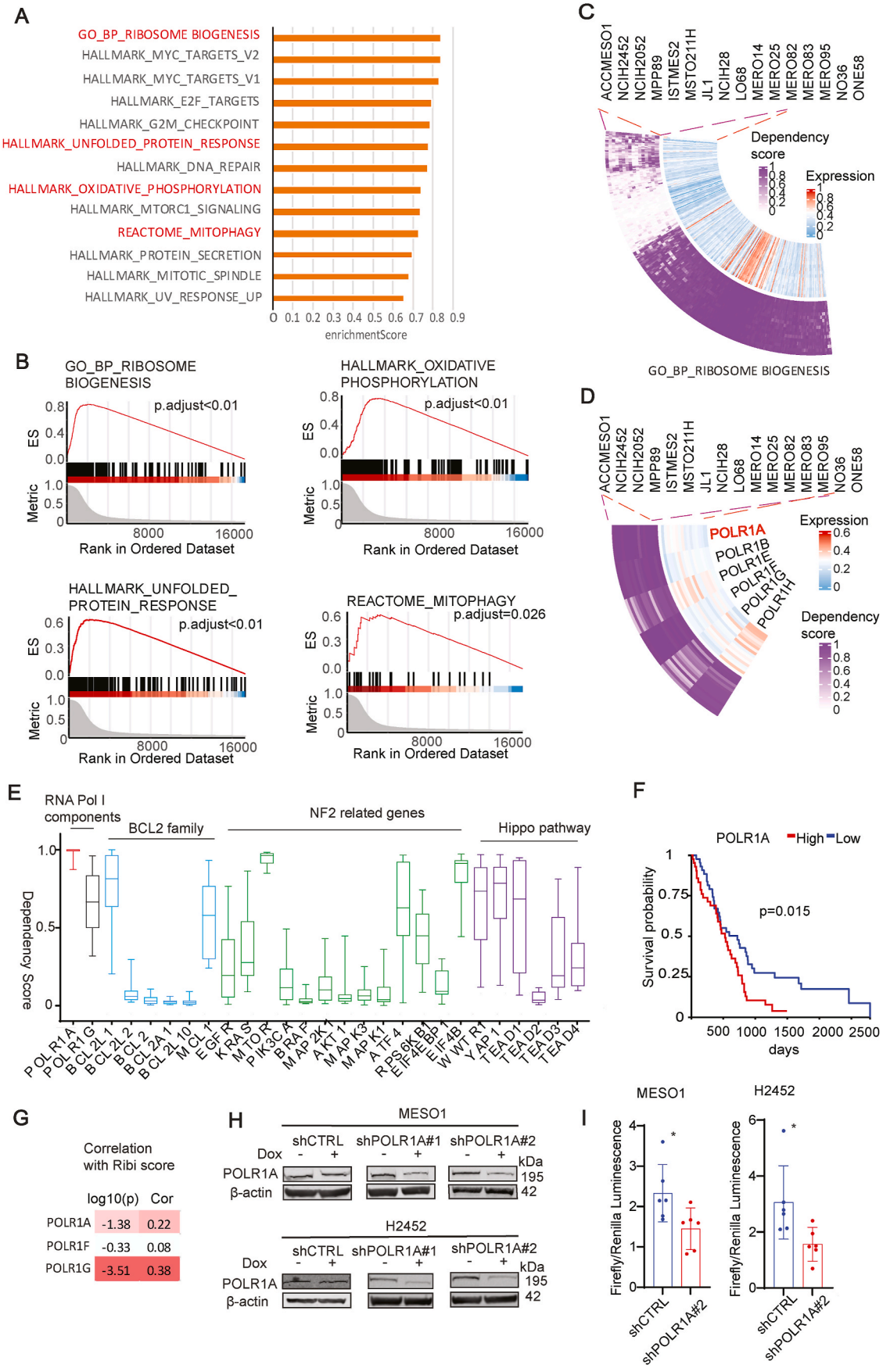

(caption on next page)

Fig. 1. POLR1A is a key genetic dependency and a potential therapeutic target in PM. **A, B.** Enrichment scores of the 13 pathways significantly over-represented across the PM dependent genes (A) and gene set enrichment analysis (GSEA) of the 4 highlighted pathways (B). The analysis was based on the CRISPR dropout dataset from the DepMap (https://depmap.org/portal/). **C.** mRNA expression and dependency scores of ribosome biogenesis genes (GO RIBOSOME BIOGENESIS gene set) across the indicated PM cell lines (n = 16). The analysis was based on the dependency and expression scores from the DepMap. **D.** mRNA expression values and dependency scores of the genes encoding RNA polymerase I subunits across the indicated PM cell lines (n = 16). The mRNA expression values and dependency scores are from Depmap. **E.** The dependency score of *PolI* subunit genes (POLR1A, POLR1G) and the previously reported genes as therapeutic targets in PM. The analysis was based on the dependency score across 16 PM cell lines from the DepMap. **F.** The expression of the *PolI* subunits POLR1A is significantly correlated with PM patient survival. Kaplan-Meier univariate survival analysis of the TCGA cohort of PM patients (n = 87) was conducted using the R 'survival' and 'survminer' packages. Patients are dichotomized by upper 50 % ($POLR1A^{high}$) and lower 50 % ($POLR1A^{low}$) of POLR1A mRNA expression. The p-value was calculated using the log-rank test. **G.** Correlation analysis of mRNA expression between POLR1A, POLR1F and POLR1G and the RiBi gene set. ssGSEA analysis was based on the TCGA-MESO dataset. Spearman correlation test is used to calculate the coefficients (Cor) and the p value. **H.** mmunoblot analysis of POLR1A knockdown in MESO1 and H2452 cells. MESO1 and H2452 cells expressing doxycycline (Dox)-inducible scramble control (shCTRL) or POLR1A-targeted shRNAs (shPOLR1A#1, shPOLR1A#2) were treated with 500 nM Dox for 48 h. **I.** Dual-luciferase reporter assay in which Firefly luciferase expression was driven by a ribosomal DNA (rDNA) promoter. After induction of shRNA targeting POLR1A (500 nM Dox for 48 h), Firefly and Renilla luciferase activities were measured, and the ratio of Firefly to Renilla luminescence was calculated to normalize for transfection efficiency. Data were presented as mean ± SD (n = 5), with ns ($p \geq 0.05$), *$p < 0.05$, **$p < 0.01$, **$p < 0.001$, ****$p < 0.0001$ by unpaired *t*-test.

SynergyFinder online tool (https://synergyfinder.org). Briefly, cells were seeded into 6-well plates (1000–2000 cells/well), treated for 96 h, and then cultured in drug-free conditions for 10–12 days, depending on the growth rate. The resulting colonies were stained with crystal violet (0.5 % in 25 % methanol).

2.7. Analysis of mitophagy with the mtKeima system

Cells transiently transfected with mKeima-Red-mito-7 (Addgene #56018) were subjected to flow cytometry using a BD FACSAria Fusion. Dual excitation of mtKeima was conducted at 408 nm (for neutral pH Keima) and 561 nm (for acidic pH Keima), corresponding to the BV605 and PE-Texas Red channels, respectively.

2.8. Mitotracker red CMX ROS assay

2×10^5 cells were seeded into 6-well dishes on day 0. On day 1, various treatments were added, and the plates were incubated at 37 °C for 48 h. Following treatment, 0.5×10^6 cells were stained in culture medium with 200 nM MitoTracker Red CMX ROS (Thermo Fisher, M46752) for 30 min at 37 °C. Cells were then washed once with PBS, suspended in PBS with 2 % FBS, and analyzed using a FACS LSR2 flow cytometer with the PE-Texas Red channel.

2.9. Seahorse assay

Cells were treated with 500 nmol/L Dox or 300 nM CX-5461 dissolved in Dimethyl Sulfoxide (DMSO) for 72 h before Seahorse assay (Aligent Seahorse XFe96/XF Pro FluxPak; 103792-100). In brief, XFE96/XF Pro Sensor Cartridge was pre-hydrated using 200 mL/well Agilent Seahorse XF Calibrant (100840-000) and XF Hydrobooster and incubated overnight at 37 °C without CO2. For an even distribution of cells, cells were detached 24 h before the assay using Trypsin-EDTA PBS 1:250 (BioConcept, 5–51F00–H) and seeded at 1 × 104 cells/well for MESO1, and 1.5 × 104 cells/well for H2452 cells in 100 ml/well of RPMI Medium 1640 (1X) with 10 % FBS and 1 % Penicillin-Streptomycin, and again 500 nmol/L Dox in an Agilent Seahorse XFe96/XF Pro Cell Culture Microplate (103794-100). 1 h prior to the Seahorse assay, media was removed and wells were washed with 100mL/well PBS, then filled with 175 ml/well of Agilent Seahorse XF RPMI Medium (103576-100) with 25 mM D-(+)-Glucose (Sigma-Aldrich, G7021) and 2 mM Stable Glutamine 100x (L-Ala-L-Gln, 200 mM) (BioConcept, 5–10K50–H), and incubated at 37 °C without CO2 for 1 h 25 mL of Oligomycin A (Tocris, 4110), Carbonyl Cyanide *m*-Chlorophenylhydrazone (Sigma-Aldrich, C2759), and Antimycin A (Sigma-Aldrich, A8674) were loaded into pores A, B, and C of the sensor cartridge at final concentrations of 2 mM, 1.5 mM, and 1.6 mM, respectively. Pore D was left empty. Then, the sensor cartridge was loaded on an Agilent Seahorse XFe96 Analyzer for calibration before XF Cell Culture Microplate was loaded into the XFe96 Analyzer, with Mito Stress Test conducted and analyzed using Wave 2.6.3.5 software (Agilent Technologies).

2.10. Public databases (TCGA, CTRP, DepMap, ChEA3) and Graphsynergy analysis for combination effects prediction

Public dataset was interrogated as we described [25]. The RNA-seq data of GSE204749 [26] and GSE145603 [27] were got from the GEO data set. Specifically, transcriptome profiling data of mesothelioma patients were obtained from the Cancer Genome Atlas (TCGA-MESO) and European Genome-phenome Archive (EGAD00001001915), and drug sensitivity data of different mesothelioma cell lines were obtained from CTRP [28,29]. The catalog of gene essentiality across PM cell lines is obtained from the Cancer Dependency Map Project (DepMap Public 24Q2) [30]. The GSEA, ssGSEA were performed by R software as previously described [31]. The Kaplan-Meier plots and Log-Rank tests were performed on the UCSC Xena according to the introduction of this website(https://xena.ucsc.edu/). The ChIP-Seq data for ATF4 in the cancer cell lines HepG2 (GSM2534290, GSM2534291) were retrieved from the Cistrome Data Browser (CistromeDB) [32]. The ATF4 motif sequence was obtained from previously published research findings [33]. The bed format files were visualized with IGV [34]. The Graphsynergy were performed according to this referred paper [35]. ChIP-X Enrichment Analysis 3 (ChEA3) is used for analyzing and ranking the TFs associated with submitted gene sets [36]. The detailed Python codes are uploaded to the github (https://github.com/Student-vector/Graphsynergy-ZT).

2.11. Single cell RNA, RNA velocity and PAGA analysis

The methods and kits used to treat the patient the samples and collect their scRNA data has been depicted in another our paper which is under the review. The raw scRNA data were uploaded to this website: https://shiny.bioinformatics.unibe.ch/apps/shiny_app_p682/. The account and password could be gotten by contacting us. The raw FASTQ reads were processed into count tables using Cell Ranger (version 6.0.1). Gene and cell filtering, dimensionality reduction and clustering were performed with Seurat (v4) [37]. Genes were kept if expressed in at least 3 cells. Cells were kept if expressed more than 500 features and less than 8000. Cells with more than 30 % of their UMI assigned to a mitochondrial gene were also removed. Principal component analysis (PCA) was performed with 2000 most variable genes. To identify tumor cells, we used inferCNV [38]. As input, we used a raw count matrix consisting of mesothelial cells, cycling mesothelial cells, endothelial cells, and fibroblasts, where the latter two cell types were used as in-sample control without copy number variation associated with cancer. The four normal samples were used as reference for inferCNV. Mesothelial cells from tumor samples that clustered together with endothelial cells or

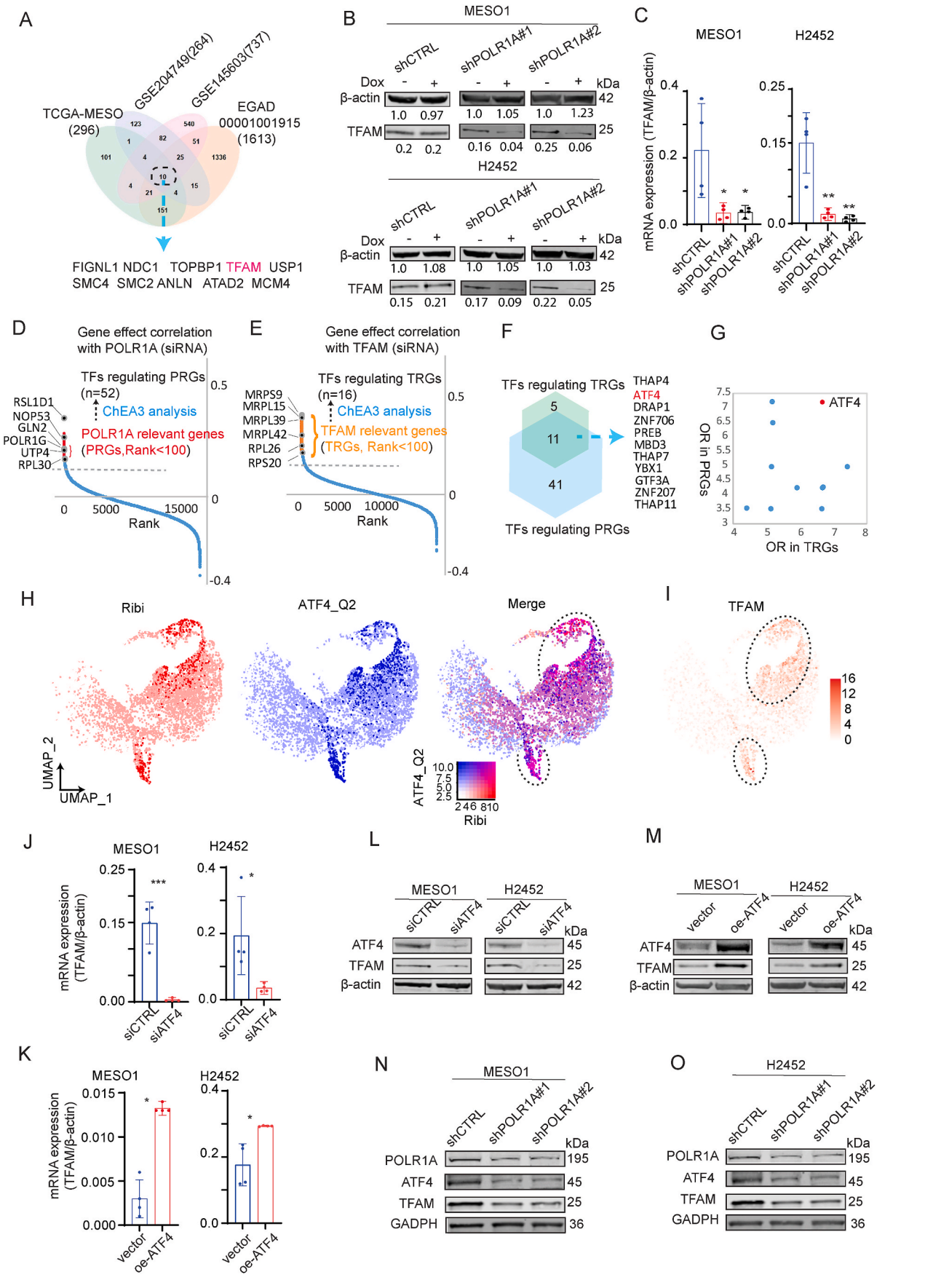

(caption on next page)

Fig. 2. POLR1A controls TFAM expression through ATF4 **A.** Venn diagram of common differentially expressed genes (DEGs) in POLR1A^{high} samples and POLR1A inhibitor-treated cell lines. DEGs were defined as those with a fold change (FC) > 1.5 and $p < 0.05$, determined using the *limma* package in R. The analysis incorporated four publicly available transcriptomic datasets: TCGA-MESO, EGAD00001001915, GSE145603, and GSE204749. Ten overlapping DEGs were identified across all datasets. **B.** Immunoblot analysis of MESO1 and H2452 cells expressing Dox-inducible shCTRL or shPOLR1A after 48h treatment with 500 nM Dox. Densitometric quantification of TFAM normalized to β-actin is shown beneath each band. **C.** Quantitative RT-PCR of MESO1 and H2452 cells expressing Dox-inducible shCTRL or shPOLR1A after 48h treatment with 500 nM Dox. Data are shown as mean ± SD (n = 4), with ns ($p \geq 0.05$), *$p < 0.05$, **$p < 0.01$, **$p < 0.001$, ****$p < 0.0001$ by unpaired *t*-test. **D, E,** Genetic co-dependency analysis identifies POLR1A- and TFAM-relevant gene sets (PRGs; TRGs). Co-dependency analysis was performed using RNAi datasets from DepMap (Achilles + DRIVE + Marcotte, DEMETER2). The X-axis represents gene rank based on correlation with POLR1A (D) or TFAM (E), while the Y-axis shows Pearson correlation coefficients of gene effect scores. Genes above the dashed line exhibit significant positive correlations ($p < 0.05$). The top 100 positively correlated genes (rank <100) are highlighted in red (PRGs) and orange (TRGs) and were subjected to transcription factor (TF) enrichment analysis using ChEA3. **F, G,** TF enrichment analysis of PRGs and TRGs identifies ATF4 a key mediator linking POLR1A and TFAM. Venn diagram showing 11 TFs commonly enriched in both PRGs and TRGs, based on ChEA3 analysis (F). Odds ratio (OR)-based enrichment analysis identifies ATF4 as the top-ranked shared TF, suggesting it may function as a key upstream regulator of both gene sets (G). **H.** UMAP visualization of coordinated RiBi and ATF4 activity in single PM cells. UMAP projections of scRNA-seq data from treatment-naïve PM samples (n = 3), with each cell scored by ssGSEA for RiBi (red gradient; GO_Ribosome_Biogenesis) and ATF4 transcriptional activity (blue gradient; ATF4_Q2 gene set, https://www.gsea-msigdb.org/gsea/msigdb/cards/ATF4_Q2). The merged overlay (bright pink) highlights cells with high scores in both pathways. **I.** UMAP visualization of TFAM expression mirrors RiBi and ATF4 activity in PM single cells. Using the same scRNA-seq dataset as in (H), cells are colored by ssGSEA scores for TFAM mRNA levels, revealing a spatial distribution that parallels high RiBi and ATF4 activity. **J, K.** qRT-PCR analysis of MESO1 and H2452 cells after transiently transfected with control (siCTRL) or ATF4-targeted siRNA (siATF4) for 48 h (J), with empty vector (vector) or ATF4 overexpression plasmid (oe-ATF4) for 48 h (K). Data are shown as mean ± SD (n = 4), with ns ($p \geq 0.05$), *$p < 0.05$, **$p < 0.01$, **$p < 0.001$, ****$p < 0.0001$ by unpaired *t*-test. **L, M.** Immunoblot analysis of POLR1A–ATF4–TFAM axis perturbations. MESO1 and H2452 cells were transiently transfected with siCTRL or siATF4 for 48 h (L), with or without ATF4 overexpression (oe-ATF4) (M). **N, O.** MESO1 and H2452 cells expressing Dox-inducible shCTRL or shPOLR1A after 48h treatment with 500 nM Dox.

fibroblasts based on the CNV profile were annotated as non-tumor, whereas all other mesothelial cells were considered tumor cells. For visualization, data was integrated using a reciprocal PCA (RPCA) dimensionality reduction and a Uniform Manifold Approximation and Projection (UMAP) was then generated based on the first 50 principal components from a PCA on the integrated data. UMAP visualization and cluster annotation were performed using the R packages dittoSeq and Seurat [37,39]. The RNA velocity and PAGA analysis is performed as the previous published paper instructed [40].

2.12. Lipid peroxidation measurement

Cells were seeded in 6-well plates and pre-treated with various drugs for 12 h, followed by co-treatment with RSL3 for 2 h. Subsequently, cells were incubated with 5 μM BODIPY 581/591C11 (Invitrogen) for 30 min, then washed twice with PBS, and harvested by trypsinization and centrifugation. Lipid peroxidation was assessed using a BD FACS Calibur flow cytometer (BD Biosciences) with a 488 nm laser and an FL1 detector for the oxidized probe. Oxidation of the polyunsaturated butadienyl portion of C11-BODIPY causes a shift in fluorescence emission from ~590 nm to ~510 nm, which is proportional to lipid ROS generation. A minimum of 10,000 single cells were analyzed per well, and three independent biological replicates were performed for each condition.

2.13. Intracellular Fe2+ measurement by flow cytometry

RhoNox-1, a fluorescent probe specific for Fe^{2+}, were used to determine intracellular Fe^{2+} levels. Following cell washing with PBS, 5 μM RhoNox-1 (MKbio, MX4558) was added to the cell suspension, and the cells were incubated at 37 °C for 1 h in the dark. The FeRhoNox-1 probe reacts with Fe^{2+} inside the cells, producing an irreversible orange-red fluorescent substance (absorption maximum, 540 nm; emission maximum, 575 nm). After a subsequent wash with PBS, fluorescence was analyzed using a Fortessa flow cytometer (BD Biosciences). The fluorescence intensity was proportional to the concentration of Fe^{2+} within the cells.

2.14. Mitochondrial Fe2+ measurement by flow cytometry

Mito-FerroGreen (M489-10, Dojindo) were used to determine mitochondrial Fe^{2+} levels. Cells were washed three times with HBSS, incubated with 5 μM Mito-FerroGreen for 30 min at 37 °C, 5 % CO2 in an incubator, and then washed three times with HBSS for flow cytometry.

2.15. Immunoblotting assay and immunochemistry assay

Immunoblots were performed as described [22]. In brief, protein lysates were resolved by SDS-PAGE (Cat. #4561033; Bio-Rad Laboratories) and transferred onto nitrocellulose membranes (Cat. #170–4158; Bio-Rad). After incubation with blocking buffer (Cat. #927–4000; Li-COR Biosciences) for 1 h at room temperature, membranes were incubated with primary antibodies at 4 °C overnight followed by secondary antibodies (1:10000 dilutions) and signal visualization.

Immunohistochemical study was performed as we described previously [25]. In brief, surgically removed xenograft tumors were formalin-fixed and paraffinembedded (FFPE). FFPE tumors were sectioned at 4 μm, deparaffinized, rehydrated and subsequently stained with and appropriate antibodies using the automated system BOND RX (Leica Biosystems, Newcastle, UK). Visualization was performed using the Bond Polymer Refine Detection kit (Leica Biosystems) as instructed by the manufacturer. Images were acquired using PANNORAMIC® whole slide scanners, processed using Case Viewer (3DHISTECH Ltd.). The staining intensities of the whole slide (two tumors/group) were quantified by ImageJ. The expression level of different groups are quantified according to the data calculated by ImageJ (integrated density/area).

2.16. In vivo mouse study

Mouse experiments were conducted in accordance with the Institutional Animal Care and Use Committee (IACUC) approved guidelines and protocols. Experiments were performed using 8-week-old male NSG (NOD-scid IL2Rγnull) mice. The sample size was determined based on preliminary experiments rather than statistical methods. Group allocation was randomized but not blinded. Suspensions of MESO-1/H2452 cells, mixed 1:1 with Matrigel (Cat. #356231; Corning), were subcutaneously inoculated into the flanks of the mice at a density of 5×10^6 cells per injection. Ten days after injection, mice were randomized to four groups ($n \geq 3$ per group): (1) shCTRL; (2) shGPX4; (3) CX-5461; (4) combination of CX-5461 and shGPX4.

For MESO1 sgCTRL/sgGPX4 cells, ten days after injection, mice were randomized to six groups ($n \geq 7$ per group): (1) sgCTRL; (2) sgGPX4; (3) sgCTRL + CX-5461; (4) sgGPX4 + CX-5461; (5) sgGPX4 + Liproxstatin-1; (4) sgGPX4 + CX-5461+ Liproxstatin-1. Tumor size was measured using a digital caliper every 2–3 days, with tumor volume calculated as follows: length × width × (length + width)/2. CX-5461 (40 mg/kg) was administrated orally every two days. Liproxstatin-1 (5 mg/kg) was administrated by intraperitoneal injection every day.

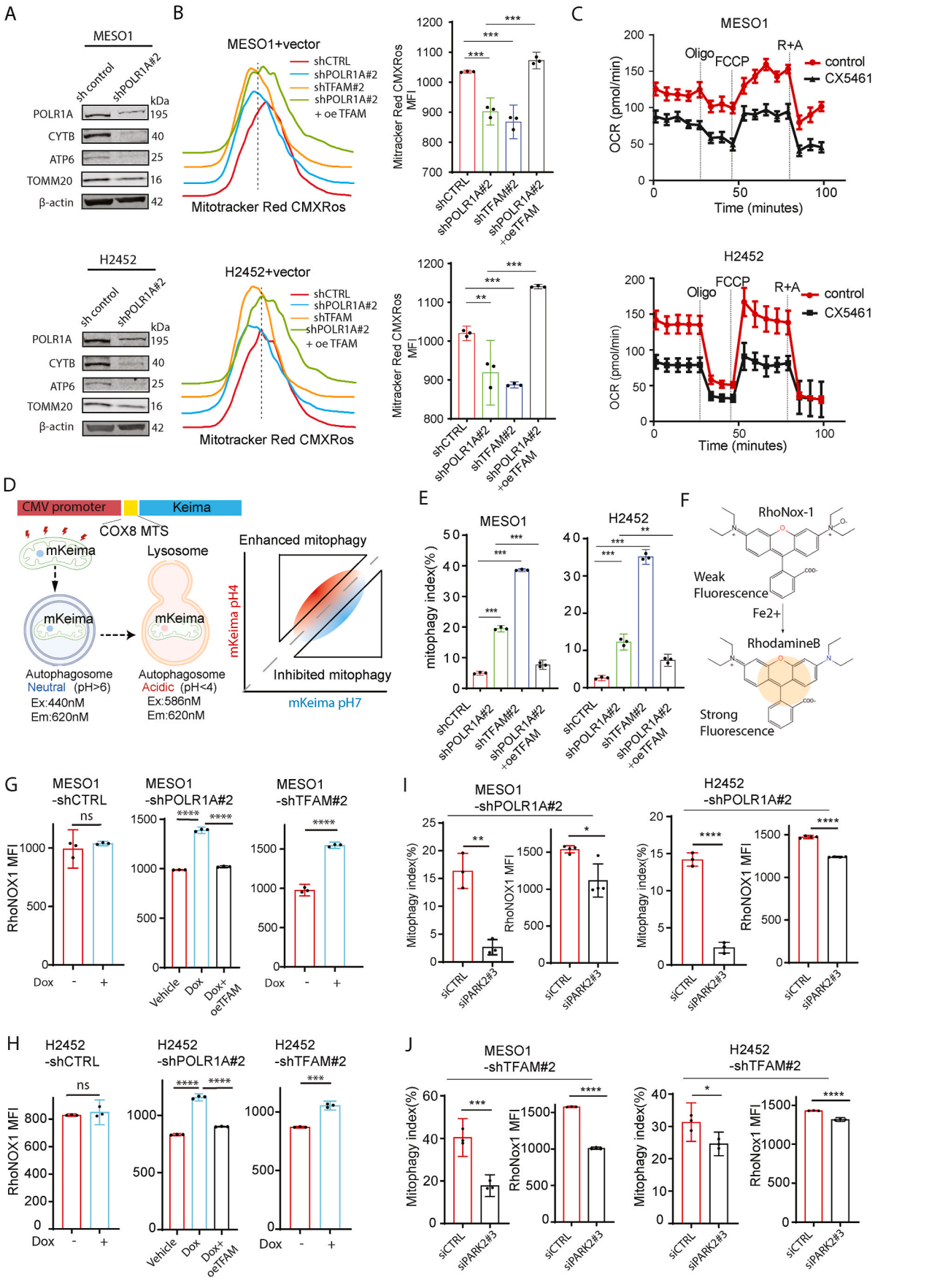

(caption on next page)

Fig. 3. The POLR1A/TFAM axis regulates mitophagy-dependent iron metabolism in PM cells. **A.** Immunoblot analysis of MESO1 and H2452 cells expressing Dox-inducible shCTRL or shPOLR1A after treated with 500 nM Dox for 48 h. **B.** The POLR1A–TFAM axis regulates mitochondrial membrane potential (Δψm). MESO1 and H2452 cells expressing Dox-inducible shCTRL, shPOLR1A, or shTFAM, with or without TFAM co-expression, were treated with 500 nM Dox for 48 h and stained with MitoTracker Red CMXRos to measure Δψm (left). Mean fluorescence intensity (MFI) was quantified as mean ± 95 % confidence interval (CI) from three independent experiments (right), with $^{**}p < 0.01$, $^{***}p < 0.001$ by unpaired two-tailed *t*-test. **C.** CX-5461 reduces oxygen consumption rate (OCR) in MESO1 and H2452 cells. Cells were treated with vehicle or 100 nM CX-5461 for 72 h. OCR was measured using a Seahorse analyzer. Data are shown as mean ± SD from at least three independent experiments (n > 3). **D.** Schematic of mt-Keima–based mitophagy reporter. The mt-Keima construct targets the pH-sensitive Keima fluorescent protein to the mitochondrial matrix. Upon delivery to acidic lysosomes, Keima's excitation shifts from 440 nm to 586 nm. The mitophagy index (%) is calculated as follows: (number of cells in the enhanced mitophagy gate/total cell number)*100. **E.** Quantification of mitophagy using the mt-Keima reporter. MESO1 and H2452 cells expressing Dox–inducible constructs, with or without TFAM co-expression, were treated with 500 nM Dox for 48 h. Mitophagy index was determined by flow cytometry using the mt-Keima reporter. Data are shown as mean ± 95 % confidence interval (CI) from three independent experiments (n = 3), with $^{**}p < 0.01$, $^{***}p < 0.001$ by unpaired two-tailed *t*-test. **F.** Chemical structure and detection mechanism of RhoNox-1, a fluorescent probe that selectively reacts with labile Fe^{2+} to generate an irreversible red-orange fluorescent product (Ex/Em: 540/575 nm). Upon binding Fe^{2+}, the probe undergoes a chemical transformation that shifts its fluorescence emission, enabling sensitive and specific detection of intracellular ferrous iron levels. **G, H.** KD of POLR1A/TFAM axis increases labile Fe^{2+} levels in PM cells. MESO1 (G) and H2452 (H) cells expressing shCTRL, shPOLR1A, or shTFAM, with or without TFAM co-expression, were treated with 500 nM Dox for 48 h, stained with RhoNox-1, and analyzed by flow cytometry. Mean fluorescence intensity (MFI) is presented as mean ± 95 % CI (n = 3), with ns ($p \geq 0.05$), $^{***}p < 0.001$, $^{****}p < 0.0001$ by unpaired *t*-test. **I, J.** PARK2 silencing suppresses POLR1A- and TFAM deficiency-induced mitophagy and labile Fe^{2+} accumulation. MESO1 and H2452 cells with Dox-inducible shPOLR1A or shTFAM were transfected with siCTRL or siPARK2#3 and cotreated with 500 nM Dox for 48 h. Mitophagy index was measured using the mt-Keima reporter by flow cytometry and labile Fe^{2+} levels were quantified with RhoNox-1 staining. Data are shown as MFI ±95 % CI (n = 3), with $^{*}p < 0.05$, $^{**}p < 0.01$, $^{***}p < 0.001$, $^{****}p < 0.0001$ by unpaired *t*-test.

2.17. Quantitative real-time PCR (qRT-PCR)

Total RNA was isolated and purified using RNeasy Mini Kit (Qiagen, Hilden, Germany). Complementary DNA was synthesized by the High capacity cDNA reverse transcription kit (Applied Biosystems, Foster City, CA, USA) according to manufacturer's instructions. Real time PCR was performed in triplicate on a 7500 Fast RealTime PCR System (Applied Biosystems) using TaqMan primer/probes (Applied Biosystems): TFAM (Hs00273372_s1)

and ACTB (Hs01060665_g1) used as endogenous normalization controls.

2.18. Dual-luciferase reporter assay for pre-rRNA transcription

Following 48 h of shRNA induction by Dox, 1×10^6 MESO1/H2452 cells were cotransfected with 5 μg pHrD-IRES-Luc [41] and 1 ng of a Renilla control plasmid using DMH13. Twenty-four h after plasmid transfection, cells were harvested and luminescence was measured using the Dual-luciferase Reporter Assay System (Promega E1910) following the manufacturer's instructions with a Varioskan microplate reader (Thermofischer). The ratio of pHrD-IRES-luciferase/Renilla activity was calculated in each group.

2.19. Statistical analysis

Statistical analyses were performed using GraphPad Prism 7.01 (GraphPad Software Inc., San Diego, CA, USA), unless otherwise indicated. Data are presented as mean ± standard deviation (SD) or mean ± standard error of the mean (SEM) from biological replicates (n > 3). Flow cytometry results are reported as mean fluorescence intensity (MFI) with 95 % confidence intervals (CI). Comparisons between groups were made using unpaired two-tailed Student's t-tests, one-way or two-way ANOVA, as appropriate. A p-value ≤0.05 was considered statistically significant. Kaplan–Meier survival analyses were conducted using the "survminer" and "survival" R packages, and statistical differences were assessed using the log-rank test.

3. Results

3.1. POLR1A is a critical genetic dependency and a potential therapeutic target in PM

To identify candidate therapeutic targets in PM, we examined DepMap CRISPR/Cas9 screening data across 16 PM cell lines (17,386 genes). After calculating each gene's average dependency score, we applied Gene Set Enrichment Analysis (GSEA). Of 13 significantly enriched pathways (adjusted $p < 0.05$), RiBi was most tightly associated with PM cell dependency, followed by canonical cancer hallmarks including the unfolded protein response (UPR) and two mitochondrial pathways – OXPHOS and mitophagy (Fig. 1A and B). Strikingly, over half of the genes in the RiBi gene set showed high dependency scores across these PM lines (Fig. 1C), highlighting RiBi as indispensable for PM cell survival.

RiBi is driven by *Pol*I, a 14-subunit enzyme that transcribes the 47S precursor rRNA from ribosomal DNA (rDNA), which is then processed into 18S, 5.8S, and 28S rRNAs [16,42]. Among the *Pol*I subunits (POLR1A, POLR1B, POLR1E, POLR1F, POLR1G, and POLR1H), POLR1A had the highest average dependency score—not only among *Pol*I components but also when compared with established PM targets (e.g., Hippo, mTORC1, RAS, EGFR, and BCL2 pathway genes) (Fig. 1D, E, Fig. S1A). Moreover, POLR1A mRNA was significantly upregulated in pan-cancer tumors versus normal controls (Fig. S1B) and positively correlated ($p < 0.05$) with worse overall survival in the TCGA-MESO cohort (n = 87) (Fig. 1F; Fig. S1C), highlighting its functional importance in PM pathogenesis.

As expected, POLR1A expression tracked with RiBi activity, as determined by single-sample GSEA (ssGSEA) (Fig. 1G). To further validate POLR1A's role in rRNA transcription, we used a luciferase reporter driven by the rDNA promoter [41]. Dox-inducible knockdown of POLR1A in H2452 cells significantly reduced Firefly/Renilla luciferase activity (Fig. 1H and I), confirming that POLR1A is essential for *Pol*I–mediated transcription.

Together, these data establish a critical role for POLR1A in PM and nominate it as a promising therapeutic target in this treatment-resistant malignancy.

3.2. POLR1A regulates TFAM expression through ATF4

To identify downstream effectors of POLR1A, we compared transcriptomes between $POLR1A^{high}$ versus $POLR1A^{low}$ PM tumors, and between PM cells ± POLR1A inhibitors, using four public datasets (TCGA-MESO, EGAD00001001915, GSE145603 and GSE204749). This analysis revealed ten genes, including TFAM, that were consistently upregulated in $POLR1A^{high}$ tumors and downregulated upon POLR1A inhibition (Fig. 2A, Fig. S2A–C).

Supporting a link between nucleolar POLR1A and mitochondrial TFAM, POLR1A and TFAM mRNA levels showed a significant positive correlation ($p < 0.05$) across TCGA pan-cancer samples (Fig. S2D). Furthermore, TFAM dependency scores strongly correlated with those of RiBi genes (Fig. S2E), consistent with the principle that functionally related genes often share dependency profiles [43]. Experimentally, POLR1A KD in PM cells significantly reduced TFAM mRNA and protein

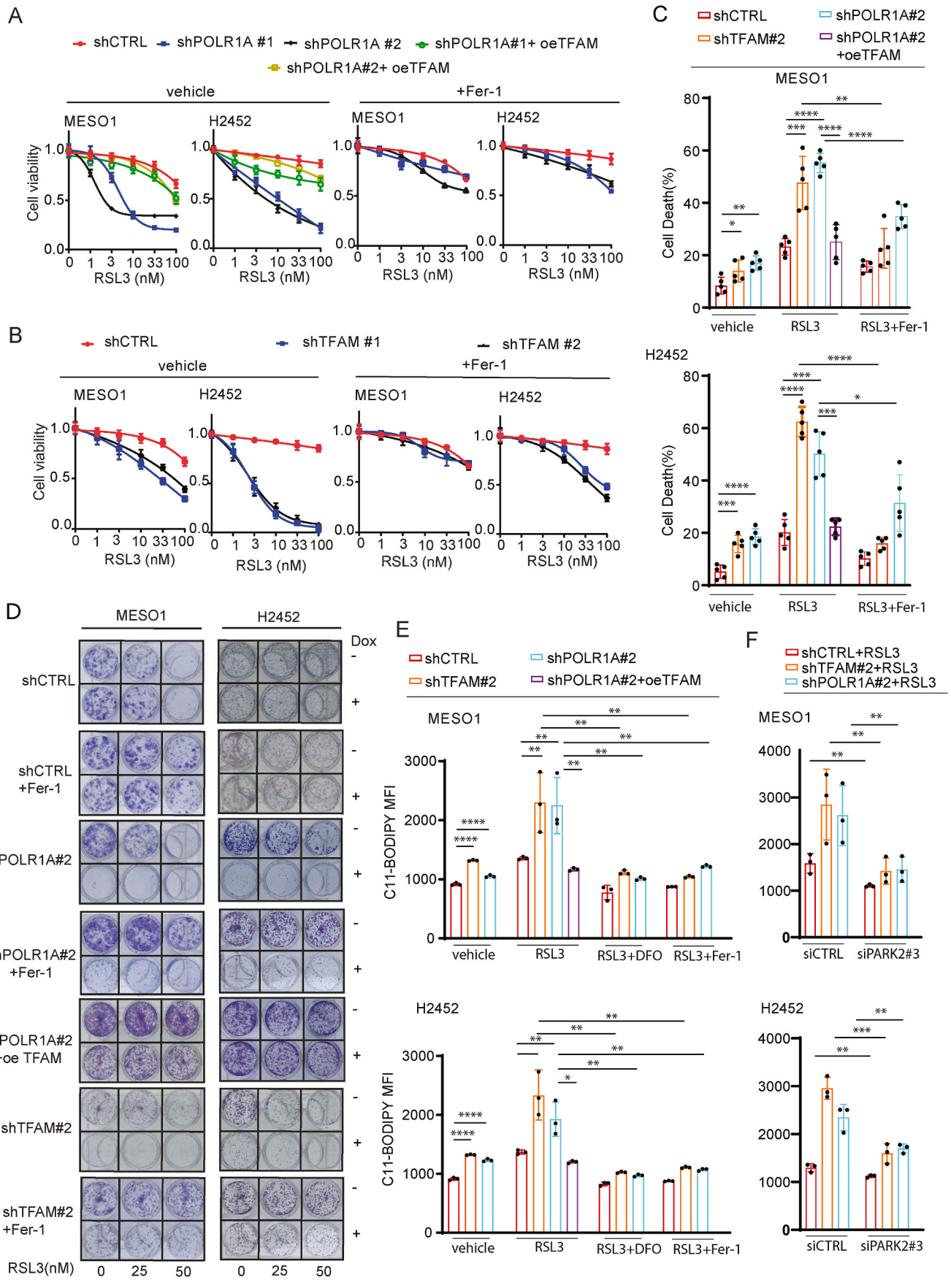

(caption on next page)

Fig. 4. The POLR1A/TFAM promotes ferroptosis resistance in PM cells **A, B.** Cell viability assay of MESO1 and H2452 cells expressing Dox–inducible shCTRL, shPOLR1A, or shTFAM, with or without TFAM overexpression (oeTFAM), after treated with 500 nM Dox and increasing concentrations of RSL3 for 48h, in the presence or absence of Fer-1 (5 μM). Data are presented as mean ± SD (n = 6). **C.** Cell death assay of MESO1 and H2452 cells expressing Dox–inducible shCTRL, shPOLR1A, or shTFAM, with or without TFAM overexpression (oeTFAM), after treated with 500 nM Dox and 200 nM RSL3 for 48h, in the presence or absence of Fer-1 (5 μM). Data are presented as mean ± SD (n = 5), with ns ($p \geq 0.05$), *$p < 0.05$, **$p < 0.01$, **$p < 0.001$, ****$p < 0.0001$ by unpaired *t*-test. **D.** Clonogenic assay of MESO1 and H2452 cells with Dox-inducible shCTRL, shPOLR1A, or shTFAM, with or without TFAM overexpression (oeTFAM), after treated with Dox (500 nM) and increasing concentrations of RSL3 for 48h, in the presence or absence of 5 μM Fer-1. **E.** MESO1 and H2452 cells expressing Dox–inducible shCTRL, shPOLR1A, or shTFAM were treated with Dox (500 nM) and RSL3 (100 nM) for 48 h, with or without TFAM overexpression (oeTFAM) and in the presence or absence of deferoxamine (DFO; 5 μM) and Fer-1 (5 μM). Lipid peroxidation was quantified by C11-BODIPY staining and flow cytometry. Data are presented as MFI ±95 % CI (n = 3), with ns ($p \geq 0.05$), *$p < 0.05$, **$p < 0.01$, **$p < 0.001$, ****$p < 0.0001$ by unpaired *t*-test. **F,** PARK2 silencing suppresses POLR1A- and TFAM deficiency-induced lipid peroxidation. MESO1 and H2452 cells with Dox-inducible shPOLR1A or shTFAM were treated with 500 nM Dox for 48 h, in the presence or absence of siPARK2. Lipid peroxidation was quantified by C11-BODIPY staining and flow cytometry. Data are shown as MFI ±95 % CI (n = 3), with ***$p < 0.001$; ****$p < 0.0001$ by unpaired *t*-test.

levels (Fig. 2B and C), indicating that POLR1A controls TFAM transcription.

To uncover intermediates linking POLR1A to TFAM, we used co-dependency mapping, an approach to identify functionally connected genes based on shared genetic dependencies [44]. From DepMap RNAi screens, we identified the top 100 genes whose KD phenotypes most closely mirrored POLR1A, defining a POLR1A-relevant gene set (PRGs; Fig. 2D). A similar analysis for TFAM generated a TFAM-relevant gene set (TRGs; Fig. 2E). Transcription factor enrichment analysis via ChIP-X Enrichment Analysis 3 (ChEA3) [36] revealed 52 candidate TFs regulating PRGs and 16 regulating TRGs (FET $p < 0.01$ for both). Eleven TFs overlapped between these lists, with ATF4 standing out given its established role in stress responses and prior reports of TFAM regulation [14] (Fig. 2F and G).

To validate a POLR1A-ATF4-TFAM axis in primary tumors, we analyzed single-cell RNA sequencing (scRNA-seq) data from treatment-naïve PM samples (n = 3; 7335 total cells; Fig. S2F). Because POLR1A and ATF4 transcripts were low in most cells, we used ssGSEA to infer pathway activity: RiBi (GO_Ribosome Biogenesis) and ATF4 transcriptional activity (ATF4_Q2 gene signature). RiBi and ATF4 scores were significantly correlated ($p < 0.05$), and cells high in both pathways also displayed elevated TFAM (Fig. 2H and I; Fig. S2G and H), reinforcing functional linkage. Interestingly, clustering based on these scores identified two cell groups - Groups A ($RiBi^{high}/ATF4^{high}$) and B ($RiBi^{low}/ATF4^{low}$) (Fig. S2G). RNA velocity and partition-based graph abstraction (PAGA) analyses showed Group A cells exhibit progenitor-like, tumor-initiating features (Fig. S2I and J), suggesting that POLR1A-ATF4-TFAM activity underlies PM progression and cellular heterogeneity.

Finally, ChIP-seq data (GSM2534290, GSM2534291) analysis revealed ATF4 binding peaks at the TFAM promoter (Fig. S2K). Consistent with this, ATF4 KD decreased and ATF4 overexpression increased TFAM mRNA (Fig. 2J and K) and protein levels (Fig. 2L and M). Moreover, POLR1A KD reduced both ATF4 and TFAM protein (Fig. 2N and O), confirming that POLR1A regulates TFAM via ATF4.

Collectively, these results establish TFAM as a direct downstream target of POLR1A through ATF4 and unveil a previously unrecognized POLR1A/TFAM axis in PM.

3.3. Inhibition of the POLR1A/TFAM axis triggers mitophagy

Given TFAM's essential role in mitochondrial function [13,45], we asked whether disrupting the POLR1A/TFAM axis impairs mitochondrial integrity. POLR1A KD reduced CYTB and ATP6 — mitochondrial-encoded OXPHOS components directly regulated by TFAM — as well as TOMM20, a nuclear-encoded component of the translocase of the outer mitochondrial membrane (Fig. 3A). Consistently, POLR1A KD lowered mitochondrial membrane potential (Δψm), as measured by MitoTracker – a defect that mirrored TFAM KD (Fig. 3B; Fig. S3A). Importantly, TFAM overexpression fully restored Δψm in POLR1A-deficient cells (Fig. 3B; Fig. S3B), confirming that TFAM mediates POLR1A's effect on mitochondrial homeostasis.

In line with these observations, both POLR1A KD and pharmacological inhibition with CX-5461 significantly decreased oxygen consumption rate (OCR) and TFAM protein levels in MESO1 and H2452 cells (Fig. 3C; Fig. S3C–E). Together, these data demonstrate that POLR1A sustains mitochondrial function through TFAM.

Because mitochondrial dysfunction often activates mitophagy [46,47], we next investigated whether POLR1A inhibition triggers this pathway. Pan-cancer TCGA analysis revealed a negative correlation between POLR1A and MAP1LC3A (a mitophagy marker), and between TFAM and PINK1 (a key mitophagy effector) (Fig. S3F). Supporting this link, POLR1A KD increased LC3A/B I and II levels, indicating enhanced autophagic flux (Fig. S3G).

To measure mitophagy directly, we utilized the mtKeima reporter system, which quantifies mitophagic flux based on Keima's pH-sensitive excitation shift: it fluoresces at 440 nm in mitochondria ($pH > 6$) and at 586 nm in acidic lysosomes ($pH < 4$) [48](Fig. 3D). Both TFAM KD and POLR1A KD significantly increased mitophagy in PM cells, and this effect was reversed by TFAM overexpression (Fig. 3E; Fig. S3H and I). These results indicate that the POLR1A-TFAM axis suppresses mitophagy under steady-state conditions to maintain mitochondrial stability.

3.4. The POLR1A/TFAM axis regulates mitophagy-dependent iron metabolism

Since mitophagy can release labile Fe^{2+} from mitochondria into the cytosol [49], we evaluated whether disrupting the POLR1A–TFAM axis alters iron homeostasis. TCGA pan-cancer analysis revealed a negative correlation between TFAM and ferritin light chain (FTL) expression (Fig. S3J), implying that low TFAM may coincide with increased ferritin turnover. Consistent with this, immunoblotting showed that KD of either POLR1A or TFAM elevated FTL and NCOA4 levels —NCOA4 being the cargo receptor for ferritinophagy, the selective degradation of ferritin to release iron (Fig. S3K–M).

To quantify intracellular Fe^{2+} directly, we employed the fluorescent probe RhoNox-1, which produces an irreversible red-orange signal (Ex/Em: 540/575 nm) upon reacting with Fe^{2+} (Fig. 3F). Both POLR1A KD and TFAM KD significantly increased labile Fe^{2+} in MESO1 and H2452 cells, and TFAM overexpression restored Fe^{2+} to baseline levels (Fig. 3G and H). Furthermore, silencing PARK2 — an E3 ubiquitin ligase essential for mitophagy — rescued the elevated mitophagy and Fe^{2+} accumulation induced by POLR1A or TFAM KD (Fig. 3I and J; Fig. S3N and O). Notably, mitochondrial Fe^{2+} levels, measured using MitoFerro-Green, were also elevated in POLR1A-deficient cells and were similarly reduced by PARK2 KD (Fig. S3P).

Collectively, these findings reveal that the POLR1A–TFAM axis preserves both mitochondrial and iron homeostasis by limiting excessive mitophagy and preventing the release of mitochondrial Fe^{2+}, thereby protecting PM cells from oxidative stress.

3.5. The POLR1A/TFAM axis promotes ferroptosis resistance

Having shown that the POLR1A/TFAM axis limits mitophagy and labile Fe^{2+}—a redox-active ion that drives lipid peroxidation via Fenton

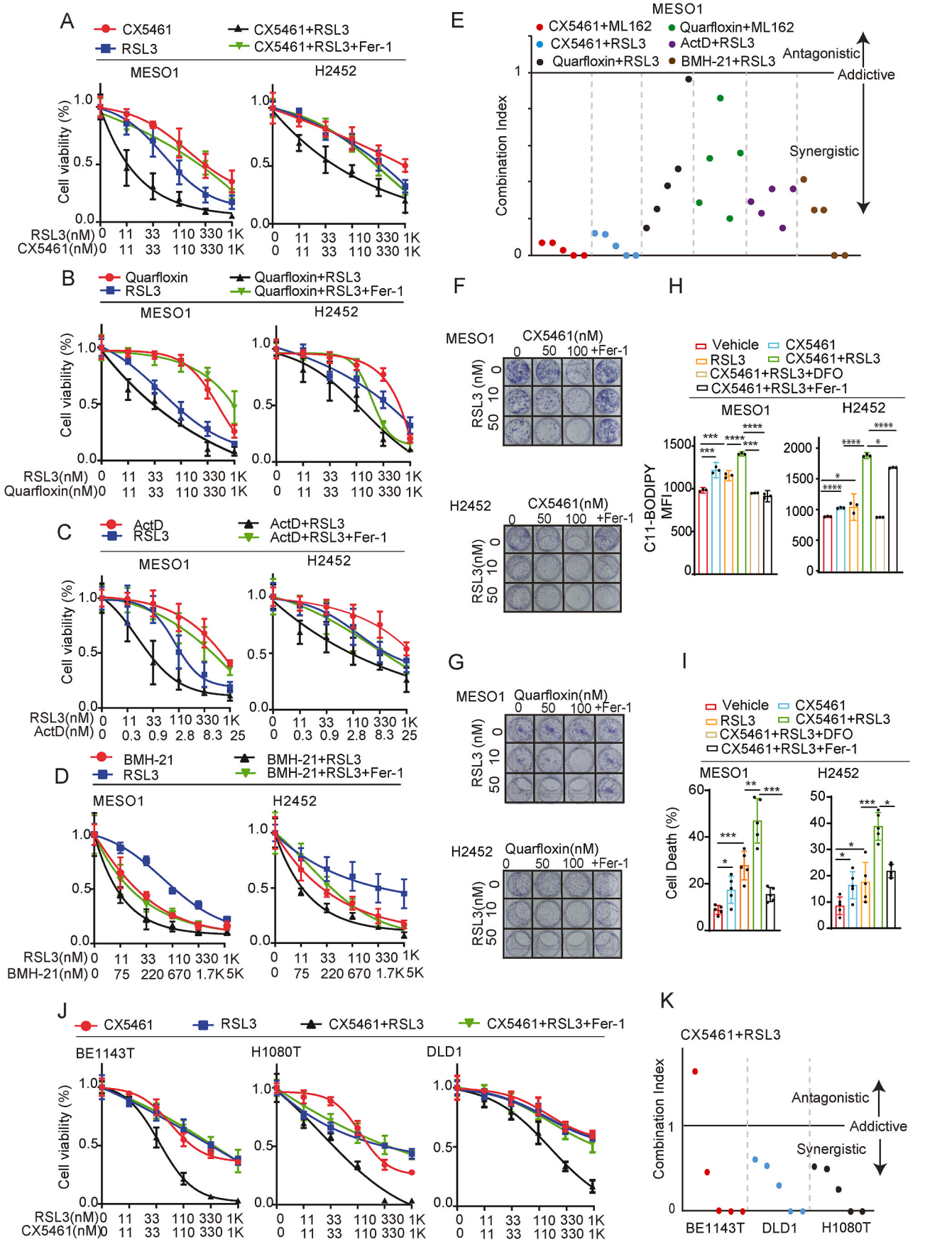

(caption on next page)

Fig. 5. RNA *PolI* suppression sensitizes PM and diverse cancer cells to GPX4 inhibition–induced ferroptosis **A-D.** Cell viability assay of MESO1 and H2452 cells treated for 48 h with increasing concentrations of RNA *PolI* inhibitors (CX-5461, quarfloxin, BMH-21, actinomycin D) and RSL3, either alone or in combination, in the presence or absence of Fer-1 (5 μM). Data are presented as mean ± SD (n = 6). **E.** Combination index (CI) analysis for RNA *PolI* and GPX4 inhibitor pairs in MESO1 cells. CI values were derived from cell viability data shown in Fig. 5A–D and Fig. S5A–B, using the Loewe additivity model. In this analysis, CI < 1 indicates synergy, CI = 1 indicates additivity, and CI > 1 indicates antagonism between a given RNA *PolI* inhibitor (e.g., CX-5461, quarfloxin, BMH-21, actinomycin D) and a GPX4 inhibitor (RSL3 or ML162). **F, G.** Clonogenic assay of MESO1 and H2452 cells treated for 48h with increasing RNA *PolI* inhibitors (CX-5461, quarfloxin) and RSL3, either alone or in combination, in the presence or absence of Fer-1 (5 μM). **H, I.** Lipid peroxidation (H) and cell death assay (I) of MESO1 and H2452 cells treated with CX-5461 (100 nM) and RSL3 (200 nM) for 48 h, in the presence or absence of Fer-1 (5 μM) and DFO (0.5 μM). Lipid peroxidation was quantified by C11-BODIPY staining and flow cytometry. Data are presented as MFI ±95 % CI (n = 3), with ns ($p \geq 0.05$), *$p < 0.05$; **$p < 0.01$; **$p < 0.001$; ****$p < 0.0001$ by unpaired *t*-test. **J.** Broad-spectrum synergy between CX-5461 and RSL3 across multiple cancer types. Primary PM cells (BE1143T), sarcoma (H1080), and colon cancer (DLD1) lines were treated with CX-5461 and RSL3 for 48 h. Combined treatment significantly reduced cell viability compared with single agents. Fer-1 (5 μM) reversed these effects. Data represent mean ± SD (n = 6). **K.** CI values for CX-5461 plus RSL3 in BE1143T, DLD1, and H1080T cells. The analysis was based on the results shown in Fig. 5J.

chemistry [50–52] —we next asked whether this pathway governs ferroptosis sensitivity in PM.

When treated with RSL3 (a GPX4 inhibitor), it produced stronger anti-tumor effects—greater loss of cell viability, impaired colony formation, and increased cell death—in POLR1A KD and TFAM KD cells compared to controls. Ferrostatin-1 (Fer-1) or TFAM overexpression rescued these effects (Fig. 4A–D, Fig. S4A–D), confirming that disrupting the POLR1A-TFAM axis sensitizes PM cells to ferroptosis.

Similarly, when treated with RSL3, POLR1A- or TFAM-depleted MESO1 and H2452 cells exhibited significantly higher lipid peroxidation—measured by C11-BODIPY fluorescence—than control cells. This lipid ROS increase was abolished by Fer-1, the iron chelator deferoxamine (DFO), or TFAM overexpression (Fig. 4E). Importantly, PARK2 KD significantly reduced RSL3-induced lipid peroxidation in POLR1A- and TFAM-deficient cells (Fig. 4F), demonstrating that the POLR1A–TFAM axis prevents ferroptosis by limiting mitophagy-driven Fe^{2+} release and subsequent lipid peroxidation (Fig. 3).

In support of these findings, Cancer Therapeutics Response Portal (CTRP) data showed that the GPX4 inhibitors RSL3 and ML162 ranked among the top 35 most cytotoxic compounds to PM cell lines, based on area under the curve (AUC) values across 16 models (Fig. S4E), highlighting GPX4 as a critical vulnerability. Computational modeling with GraphSynergy predicted strong synergy between POLR1A inhibition and GPX4 blockade in MESO1 and H2452 cells—two lines that also exhibited greater sensitivity to multiple GPX4 inhibitors (RSL3, ML162) relative to other PM models (Fig. S4F and G).

Interestingly, POLR1A KD upregulated SLC7A11 in MESO1 and H2452 cells yet did not sensitize them to erastin—a ferroptosis inducer targeting SLC7A11 and activating voltage-dependent anion channels (VDACs) (Fig. S4H and I). Whether POLR1A confers ferroptosis resistance via an SLC7A11-independent mechanism warrants further investigation.

Together, these data establish the POLR1A–TFAM axis as a key regulator of ferroptosis resistance in PM. By suppressing mitophagy and preventing labile Fe^{2+} release, this pathway shields cells from iron-dependent lipid peroxidation and ferroptotic death. Disrupting the axis sensitizes PM cells to ferroptosis inducers, offering a promising strategy to overcome resistance and improve therapeutic outcomes in mesothelioma.

3.6. *POL I inhibition synergizes with GPX4 blockade to induce ferroptosis in vitro and in vivo*

To translate our mechanistic insights into a therapeutic strategy, we tested several *PolI* inhibitors—actinomycin D, BMH-21, quarfloxin, and CX-5461 — for their ability to enhance ferroptosis. All four compounds demonstrated synergistic cytotoxicity when combined with RSL3 or ML162 in MESO1 and H2452 cell lines, reducing viability more effectively than either agent alone (Fig. 5A–E; Fig. S5A–C). The combinatorial effect was similarly observed in clonogenic assay, lipid peroxidation and cell death assays and this synergy was abolished by co-treatment with Fer-1 (Fig. 5F–I), confirming ferroptosis dependence.

Importantly, the same combinatorial effect occurred in BE1143T (primary PM cells), H1080 (sarcoma), and DLD1 (colon cancer) cell lines (Fig. 5J, K, Fig. S5D and E), indicating broad anti-tumor potential that extended beyond PM.

For in vivo validation, we selected CX-5461 (Pidnarulex), a first-in-class *PolI* inhibitor with demonstrated activity and tolerability in clinical trials [19–21], and combined it with GPX4 KD and knockout (KO) (Fig. S6A–C). While either GPX4 KD or CX-5461 alone modestly slowed tumor growth, their combination produced a significantly enhanced anti-tumor effect without observable toxicity or weight loss (Fig. S6D and E). Likewise, MESO1 tumors harboring GPX4 KO plus CX-5461 showed pronounced growth inhibition that was reversed by Lip-1 (Fig. 6A–C), confirming ferroptosis as the primary mechanism.

Immunohistochemical analysis demonstrated that combining CX-5461 with GPX4 knockdown markedly decreased Ki67 staining relative to either treatment alone (Fig. 6D–F), consistent with reduced tumor cell proliferation. Although CX-5461 is known to induce DNA damage [20,21], γ-H2AX levels did not increase further when CX-5461 was paired with GPX4 inhibition (Fig. 6F). This finding was corroborated by in vitro immunoblots showing that co-treatment with CX-5461 and RSL3 minimally affected γ-H2AX and p53 levels compared to single-agent treatments (Fig. 6G). Together, these data confirm that the synergistic antitumor activity of *PolI* inhibition and GPX4 blockade operates independently of DNA damage and is instead mediated by ferroptotic cell death.

In summary, our in vitro and in vivo studies establish that combining GPX4 inhibition with POLR1A targeting via CX-5461 creates a potent ferroptosis-based therapy for pleural mesothelioma. This approach heightens ferroptotic sensitivity, suppresses tumor growth, and may overcome therapy resistance in mesothelioma and other ferroptosis-refractory cancers.

4. Discussion

Ferroptosis has emerged as a promising therapeutic vulnerability in cancer, yet the molecular mechanisms underlying ferroptosis sensitivity and resistance remain incompletely understood. In this study, we uncover a previously unrecognized POLR1A/TFAM axis that regulates mitophagy, maintains iron homeostasis, and suppresses ferroptosis in PM and other cancers. Importantly, we show that pharmacological inhibition of POLR1A using the RNA *PolI* inhibitor CX-5461 synergizes with GPX4 blockade to enhance ferroptotic cell death in vitro and in vivo, suggesting a new therapeutic strategy for overcoming ferroptosis resistance (Fig. 7).

POLR1A is traditionally recognized for its essential role in ribosomal RNA transcription and RiBi [16,18]. Our findings extend this role by identifying POLR1A as a key upstream regulator of mitochondrial homeostasis and ferroptosis susceptibility. We demonstrate that POLR1A drives ATF4-dependent transcription of TFAM, the master regulator of mitochondrial DNA maintenance and oxidative phosphorylation [13]. By sustaining TFAM expression, POLR1A restrains excessive mitophagy, thereby limiting the liberation of mitochondrial Fe^{2+} and downstream

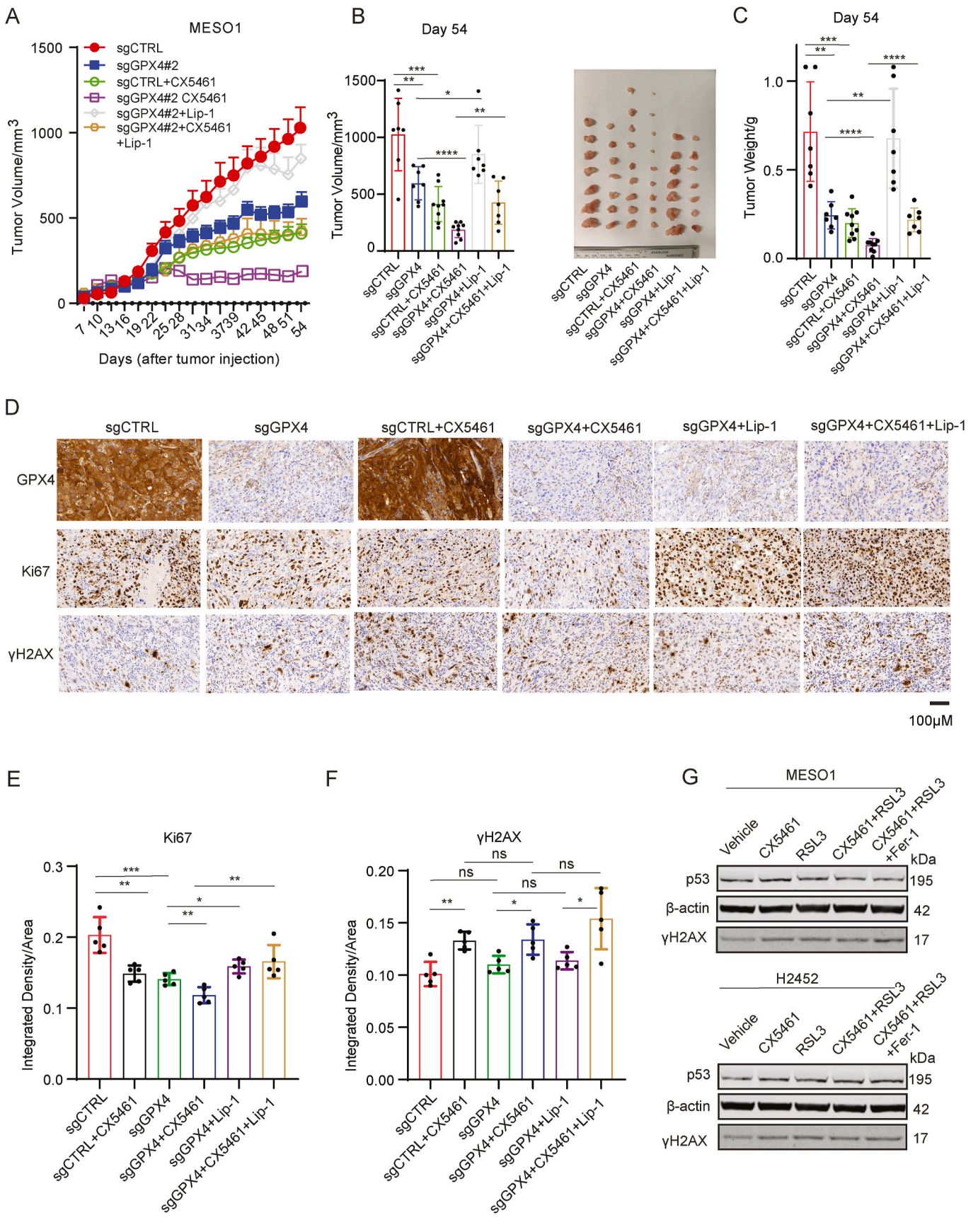

(caption on next page)

Fig. 6. CX-5461 suppresses in vivo growth of GPX4-deficient PM tumors **A,** Tumor growth curves of MESO1 xenografts in NSG mice (7–9 mice per group) expressing control sgRNA or sgGPX4, treated with CX-5461 (40 mg/kg, oral gavage every other day), Liproxstatin-1 (5 mg/kg, intraperitoneal injection daily), or the combination for 54 days. **B, C.** Final tumor volumes (B) and weights (C) measured on day 54. Data are presented as mean ± SD. Statistical comparisons between groups were performed by unpaired two-tailed *t*-test: *p < 0.05; **p < 0.01; **p < 0.001. **D.** Immunohistochemical (IHC) analysis of MESO1 xenograft tumors. Representative IHC staining for GPX4, the proliferation marker Ki67, and the DNA damage marker γH2AX in tumor sections collected on day 54. Scale bars, 100 μm. **E, F.** Quantification of Ki67 and γH2AX staining in MESO1 xenografts. IHC images from panel D were quantified for Ki67 (E) and γH2AX (F) using integrated density normalized to tissue area. Data represent mean ± SD from five independent tumor sections per group. Statistical comparisons to vehicle-treated controls were made by unpaired two-tailed *t*-test: ns ($p \geq 0.05$), *p < 0.05; **p < 0.01; **p < 0.001. **G.** Immunoblot analysis of MESO1 and H2452 cells treated for 48 h with vehicle, CX-5461 (100 nM), and RSL3 (100 nM), either alone or in combination, in the presence or absence of Fer-1 (5 μM).

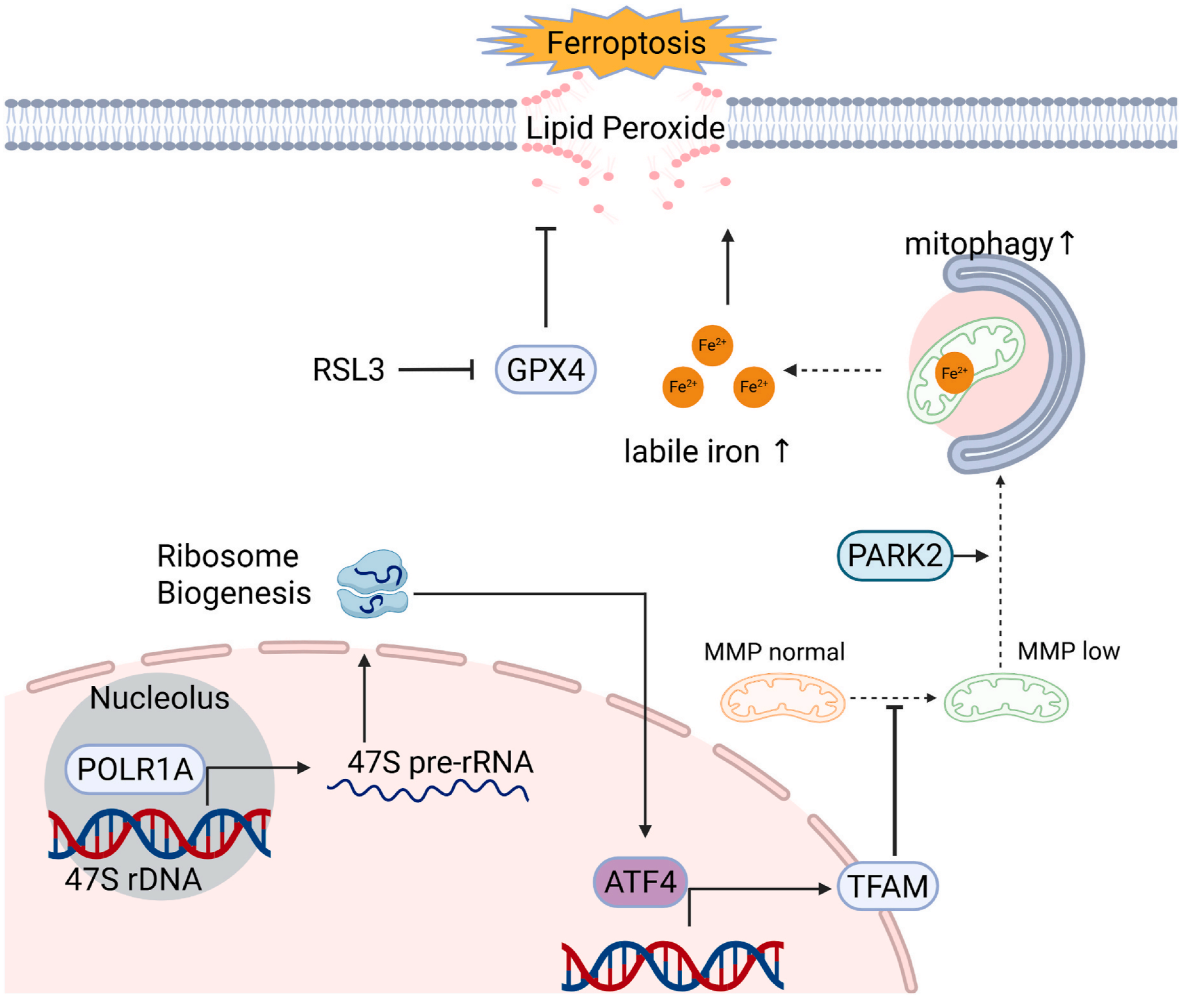

Fig. 7. Working model of the POLR1A–ATF4–TFAM axis in ferroptosis defense.
Under homeostatic conditions, POLR1A promotes ATF4–mediated transcription of TFAM, ensuring proper mitochondrial gene expression and function. TFAM supports mitochondrial integrity, limiting mitophagy and the consequent release of labile Fe^{2+}, thereby preventing iron-driven lipid peroxidation and ferroptotic cell death. Inhibition of POLR1A or disruption of ATF4–TFAM signaling triggers excessive mitophagy, elevates cytosolic Fe^{2+}, and sensitizes cancer cells to GPX4 inhibitors (e.g., RSL3), leading to hyperactivation of ferroptosis.

lipid peroxidation. These findings extend the concept of a nucleolar–mitochondrial crosstalk, linking ribosome biogenesis directly to redox homeostasis and cellular stress defenses [53,54].

Mitochondria serve as hubs for both metabolic and iron-handling processes. As sites for Fe–S cluster formation, heme biosynthesis, and mitochondrial ferritin (FTMT) storage, they are also major sources of ROS under stress. Mitophagy, the selective removal of damaged mitochondria, normally preserves redox balance and cellular health [55], but when dysregulated it paradoxically fuels ferroptosis by releasing mitochondrial Fe^{2+} into the cytosol [11,49]. Our data reveal that the POLR1A/TFAM axis acts as a critical checkpoint in this balance: by sustaining TFAM expression, POLR1A restrains excessive mitophagy and thus limits labile iron release and downstream lipid peroxidation. This context-dependent duality of mitophagy—protective at basal levels yet pro-ferroptotic when overactivated—mirrors previous reports showing that iron depletion triggers mitophagy via FTMT and NCOA4, whereas unchecked mitophagy drives Fe^{2+} accumulation and ferroptotic cell death [47,55]. Through this mechanism, POLR1A/TFAM safeguards PM cells from ferroptotic stress.

We further uncover ATF4 as a pivotal nexus between nucleolar and mitochondrial stress. Although best known for orchestrating the ER unfolded protein response [56], ATF4 also drives TFAM transcription to coordinate mitochondrial biogenesis and keep mitophagy in check [14]. Downstream of POLR1A, ATF4 thereby integrates ribosome biogenesis with mitochondrial quality control, forging a unified adaptive network that underpins ferroptosis resistance.

Therapeutically, these insights provide a compelling rationale for dual targeting of POLR1A and GPX4. CX-5461 disrupts POLR1A activity, leading to increased mitophagy and cytosolic Fe^{2+} accumulation, which sensitizes cells to ferroptosis. In this iron-rich context, cells become more dependent on GPX4 for survival. Co-inhibition of POLR1A and GPX4 therefore represents a synergistic strategy that dismantles two layers of ferroptosis resistance—iron homeostasis and antioxidant defense. Importantly, although our study focuses on PM, the POLR1A–ATF4–TFAM regulatory axis may be relevant in other cancers with elevated ribosome biogenesis activity. Targeting this axis could offer broader therapeutic opportunities across tumor types characterized by ferroptosis evasion.

In summary, we identify a novel POLR1A–TFAM signaling axis that connects nucleolar function to mitochondrial dynamics, iron regulation, and ferroptosis resistance. By showing that POLR1A inhibition sensitizes cancer cells to ferroptosis through mitophagy-dependent iron accumulation, we establish a mechanistic rationale for combining *PolI* inhibition with ferroptosis inducers. This integrated therapeutic approach opens new avenues for targeting therapy-resistant cancers through ferroptosis activation.

CRediT authorship contribution statement

Tuo Zhang: Investigation, Software, Data curation, Methodology, Writing – original draft, Formal analysis, Writing – review & editing, Conceptualization, Visualization, Validation. **Yanyun Gao:** Data curation, Methodology, Investigation, Software, Visualization, Writing – review & editing. **Marcell Harhai:** Methodology, Formal analysis, Investigation. **Alexis A. Jourdain:** Methodology, Formal analysis, Investigation. **Thomas M. Marti:** Resources, Writing – review & editing. **Erik Vassella:** Funding acquisition, Resources, Writing – review & editing. **Zhang Yang:** Conceptualization, Writing – review & editing, Investigation, Methodology. **Qinghua Zhou:** Resources, Conceptualization, Funding acquisition, Writing – review & editing. **Patrick Dorn:** Conceptualization, Writing – original draft, Resources, Funding acquisition. **Ren-Wang Peng:** Funding acquisition, Project administration, Writing – review & editing, Conceptualization, Resources, Writing – original draft.

Financial support

This work was supported by grants from the Swiss National Science Foundation (;SNSF#_310030192648 SNSF# 320030-231251 to RWP), the Bern Center of Precision Medicine (to RWP, PD & EV), Stiftung zur Krebsbekämpfung (PD), the ISREC Foundation (Lausanne, Switzerland; to RWP), the National Key Research and Development Plan of China (No 2016YEE0103400 to QZ), and by a PhD fellowship from the China Scholarship Council (to TZ).

Declaration of competing interest

The authors declare that they have no known competing financial interests or personal relationships that could have appeared to influence the work reported in this paper.

The author is an Editorial Board Member/Editor-in-Chief/Associate Editor/Guest Editor for this journal and was not involved in the editorial review or the decision to publish this article.

The authors declare the following financial interests/personal relationships which may be considered as potential competing interests.

Acknowledgements

We thank Christelle Dubey for her expert technical assistance, particularly in conducting the animal studies. We also acknowledge the Translational Research Unit at the Institute of Tissue Medicine and Pathology, University of Bern, for performing the immunohistochemistry (IHC); the Next Generation Sequencing (NGS) Platform; the Flow Cytometry and Cell Sorting Facility; and the Experimental Animal Center at the University of Bern for their valuable support and services.

Appendix A. Supplementary data

Supplementary data to this article can be found online at https://doi.org/10.1016/j.redox.2025.103758.

SUPPLEMENTARY INFORMATION

Supplementary data accompany this manuscript.

References

[1] M. Carbone, P.S. Adusumilli, H.R. Alexander Jr., P. Baas, F. Bardelli, A. Bononi, et al., Mesothelioma: scientific clues for prevention, diagnosis, and therapy, CA Cancer J. Clin. 69 (2019) 402–429.
[2] J. Hmeljaki, F. Sanchez-Vega, K.A. Hoadley, J. Shih, C. Stewart, D. Heiman, et al., Integrative molecular characterization of malignant pleural mesothelioma, Cancer Discov. 8 (2018) 1548–1565.
[3] R. Bueno, E.W. Stawiski, L.D. Goldstein, S. Durinck, A. De Rienzo, Z. Modrusan, et al., Comprehensive genomic analysis of malignant pleural mesothelioma identifies recurrent mutations, gene fusions and splicing alterations, Nature Genet (Article) 48 (2016) 407.
[4] D.A. Fennell, S. Dulloo, J. Harber, Immunotherapy approaches for malignant pleural mesothelioma, Nat. Rev. Clin. Oncol. 19 (2022) 573–584.
[5] D. Xu, S.Q. Liang, M. Su, H. Yang, R. Bruggmann, S. Oberhaensli, et al., Crispr-mediated genome editing reveals a preponderance of non-oncogene addictions as targetable vulnerabilities in pleural mesothelioma, Lung Cancer 197 (2024) 107986.
[6] X.J. Jiang, B.R. Stockwell, M. Conrad, Ferroptosis: mechanisms, biology and role in disease, Nat. Rev. Mol. Cell Biol. 22 (2021) 266–282.
[7] G. Lei, L. Zhuang, B. Gan, Targeting ferroptosis as a vulnerability in cancer, Nat. Rev. Cancer 22 (2022) 381–396.
[8] J. Zheng, M. Conrad, The metabolic underpinnings of ferroptosis, Cell Metab. 32 (2020) 920–937.
[9] B. Gan, Mitochondrial regulation of ferroptosis, J. Cell Biol. 220 (2021).
[10] K. Palikaras, E. Lionaki, N. Tavernarakis, Mechanisms of mitophagy in cellular homeostasis, physiology and pathology, Nat. Cell Biol. 20 (2018) 1013–1022.
[11] S.I. Yamashita, Y. Sugiura, Y. Matsuoka, R. Maeda, K. Inoue, K. Furukawa, et al., Mitophagy mediated by BNIP3 and NIX protects against ferroptosis by downregulating mitochondrial reactive oxygen species, Cell Death Differ. 31 (2024) 651–661.
[12] P. Yang, J. Li, T. Zhang, Y. Ren, Q. Zhang, R. Liu, et al., Ionizing radiation-induced mitophagy promotes ferroptosis by increasing intracellular free fatty acids, Cell Death Differ. 30 (2023) 2432–2445.
[13] H. Liu, C. Zhen, J. Xie, Z. Luo, L. Zeng, G. Zhao, et al., TFAM is an autophagy receptor that limits inflammation by binding to cytoplasmic mitochondrial DNA, Nat. Cell Biol. 26 (2024) 878–891.
[14] P.M. Quirós, M.A. Prado, N. Zamboni, D. D'Amico, R.W. Williams, D. Finley, et al., Multi-omics analysis identifies ATF4 as a key regulator of the mitochondrial stress response in mammals, J. Cell Biol. 216 (2017) 2027–2045.
[15] M. Molenaars, G.E. Janssens, E.G. Williams, A. Jongejan, J. Lan, S. Rabot, et al., A conserved mito-cytosolic translational balance links two longevity pathways, Cell Metab. 31 (2020) 549–563.e547.
[16] J. Russell, J.C. Zomerdijk, RNA-polymerase-I-directed rDNA transcription, life and works, Trends Biochem. Sci. 30 (2005) 87–96.
[17] J.A. Saba, K. Liakath-Ali, R. Green, F.M. Watt, Translational control of stem cell function, Nat. Rev. Mol. Cell Biol. 22 (2021) 671–690.
[18] J. Pelletier, G. Thomas, S. Volarević, Ribosome biogenesis in cancer: new players and therapeutic avenues, Nat. Rev. Cancer 18 (2018) 51–63.
[19] A. Khot, N. Brajanovski, D.P. Cameron, N. Hein, K.H. Maclachlan, E. Sanij, et al., First-in-Human RNA polymerase I transcription inhibitor CX-5461 in patients with advanced hematologic cancers: results of a phase I dose-escalation study, Cancer Discov. 9 (2019) 1036–1049.
[20] H. Xu, M. Di Antonio, S. McKinney, V. Mathew, B. Ho, N.J. O'Neil, et al., CX-5461 is a DNA G-quadruplex stabilizer with selective lethality in BRCA1/2 deficient tumours, Nat. Commun. 8 (2017) 14432.
[21] J. Hilton, K. Gelmon, P.L. Bedard, D. Tu, H. Xu, A.V. Tinker, et al., Results of the phase I CCTG IND.231 trial of CX-5461 in patients with advanced solid tumors enriched for DNA-Repair deficiencies, Nat. Commun. 13 (2022) 3607.
[22] D. Xu, S.Q. Liang, H. Yang, R. Bruggmann, S. Berezowska, Z. Yang, et al., CRISPR screening identifies WEE1 as a combination target for standard chemotherapy in malignant pleural mesothelioma, Mol Cancer Ther 19 (2020) 661–672.
[23] D. Xu, S.Q. Liang, Z. Yang, H. Yang, R. Bruggmann, S. Oberhaensli, et al., Malignant pleural mesothelioma co-opts BCL-XL and autophagy to escape apoptosis, Cell Death Dis. 12 (2021) 406.
[24] Z. Yang, S.Q. Liang, M. Saliakoura, H. Yang, E. Vassella, G. Konstantinidou, et al., Synergistic effects of FGFR1 and PLK1 inhibitors target a metabolic liability in KRAS-Mutant cancer, EMBO Mol. Med. 13 (2021) e13193.

[25] D. Xu, Y. Gao, H. Yang, M. Spils, T.M. Marti, T. Losmanová, et al., BAP1 deficiency inflames the tumor immune microenvironment and is a candidate biomarker for immunotherapy response in malignant pleural mesothelioma, JTO Clin Res Rep 5 (2024) 100672.
[26] C. Otto, C. Kastner, S. Schmidt, K. Uttinger, A. Baluapuri, S. Denk, et al., RNA polymerase I inhibition induces terminal differentiation, growth arrest, and vulnerability to senolytics in colorectal cancer cells, Mol. Oncol. 16 (2022) 2788–2809.
[27] C. Morral, J. Stanisavljevic, X. Hernando-Momblona, E. Mereu, A. Álvarez-Varela, C. Cortina, et al., Zonation of ribosomal DNA transcription defines a stem cell hierarchy in colorectal cancer, Cell Stem Cell 26 (2020) 845–861.e812.
[28] J. Li, Y.L. Lu, R. Akbani, Z.L. Ju, P.L. Roebuck, W.B. Liu, et al., TCPA: a resource for cancer functional proteomics data, Nat. Methods 10 (2013) 1046–1047.
[29] E. Cerami, J.J. Gao, U. Dogrusoz, B.E. Gross, S.O. Sumer, B.A. Aksoy, et al., The cBio cancer genomics portal: an open platform for exploring multidimensional cancer genomics data, Cancer Discov. 2 (2012) 401–404.
[30] A. Tsherniak, F. Vazquez, P.G. Montgomery, B.A. Weir, G. Kryukov, G.S. Cowley, et al., Defining a cancer dependency map, Cell (Article) 170 (2017) 564.
[31] T. Zhang, H.T. Ang, B.B. Sun, F. Yao, Four hub genes regulate tumor infiltration by immune cells, antitumor immunity in the tumor microenvironment, and survival outcomes in lung squamous cell carcinoma patients, Aging-US (Article) 13 (2021) 3819–3842.
[32] S. Heinz, C. Benner, N. Spann, E. Bertolino, Y.C. Lin, P. Laslo, et al., Simple combinations of lineage-determining transcription factors prime cis-regulatory elements required for macrophage and B cell identities, Molecular cell 38 (2010) 576–589.
[33] T. Örd, D. Örd, P. Adler, T. Örd, Genome-wide census of ATF4 binding sites and functional profiling of trait-associated genetic variants overlapping ATF4 binding motifs, PLoS Genet. 19 (2023) e1011014.
[34] J.T. Robinson, H. Thorvaldsdóttir, W. Winckler, M. Guttman, E.S. Lander, G. Getz, et al., Integrative genomics viewer, Nat. Biotechnol. 29 (2011) 24–26.
[35] J. Yang, Z. Xu, W.K.K. Wu, Q. Chu, Q. Zhang, GraphSynergy: a network-inspired deep learning model for anticancer drug combination prediction, J. Am. Med. Inf. Assoc. : JAMIA 28 (2021) 2336–2345.
[36] A.B. Keenan, D. Torre, A. Lachmann, A.K. Leong, M.L. Wojciechowicz, V. Utti, et al., ChEA3: transcription factor enrichment analysis by orthogonal omics integration, Nucleic Acids Res. 47 (2019) W212–W224.
[37] Y. Hao, S. Hao, E. Andersen-Nissen, W.M. Mauck 3rd, S. Zheng, A. Butler, et al., Integrated analysis of multimodal single-cell data, Cell 184 (2021) 3573–3587 e3529.
[38] T. Tickle, I. Tirosh, C. Georgescu, M. Brown, B. Haas, Infercnv of the Trinity CTAT Project. Klarman Cell Observatory, Broad Institute of MIT and Harvard, Cambridge, MA, USA, 2019.
[39] D.G. Bunis, J. Andrews, G.K. Fragiadakis, T.D. Burt, M. Sirota, dittoSeq: universal user-friendly single-cell and bulk RNA sequencing visualization toolkit, Bioinformatics 36 (2021) 5535–5536.
[40] Manno G. La, R. Soldatov, A. Zeisel, E. Braun, H. Hochgerner, V. Petukhov, et al., RNA velocity of single cells, Nature 560 (2018) 494–498.
[41] K. Ghoshal, S. Majumder, J. Datta, T. Motiwala, S. Bai, S.M. Sharma, et al., Role of human ribosomal RNA (rRNA) promoter methylation and of methyl-cpg-binding protein MBD2 in the suppression of rRNA gene expression, J. Biol. Chem. 279 (2004) 6783–6793.
[42] D. Drygin, W.G. Rice, I. Grummt, The RNA polymerase I transcription machinery: an emerging target for the treatment of cancer, Annu. Rev. Pharmacol. Toxicol. 50 (2010) 131–156.
[43] J.M. McFarland, Z.V. Ho, G. Kugener, J.M. Dempster, P.G. Montgomery, J. G. Bryan, et al., Improved estimation of cancer dependencies from large-scale RNAi screens using model-based normalization and data integration, Nat. Commun. 9 (2018) 4610.
[44] M. Wainberg, R.A. Kamber, A. Balsubramani, R.M. Meyers, N. Sinnott-Armstrong, D. Hornburg, et al., A genome-wide atlas of co-essential modules assigns function to uncharacterized genes, Nat. Genet. 53 (2021) 638–649.
[45] C.M. Gustafsson, M. Falkenberg, N.G. Larsson, Maintenance and expression of mammalian mitochondrial DNA, Annu. Rev. Biochem. 85 (2016) 133–160.
[46] F. Koyano, K. Okatsu, H. Kosako, Y. Tamura, E. Go, M. Kimura, et al., Ubiquitin is phosphorylated by PINK1 to activate parkin, Nature 510 (2014) 162–166.
[47] G.F. Allen, R. Toth, J. James, I.G. Ganley, Loss of iron triggers PINK1/Parkin-independent mitophagy, EMBO Rep. 14 (2013) 1127–1135.
[48] H. Katayama, T. Kogure, N. Mizushima, T. Yoshimori, A. Miyawaki, A sensitive and quantitative technique for detecting autophagic events based on lysosomal delivery, Chemistry & biology 18 (2011) 1042–1052.
[49] F. Yu, Q. Zhang, H. Liu, J. Liu, S. Yang, X. Luo, et al., Dynamic O-GlcNAcylation coordinates ferritinophagy and mitophagy to activate ferroptosis, Cell Discov 8 (2022) 40.
[50] S.J. Dixon, K.M. Lemberg, M.R. Lamprecht, R. Skouta, E.M. Zaitsev, C.E. Gleason, et al., Ferroptosis: an iron-dependent form of nonapoptotic cell death, Cell (Article) 149 (2012) 1060–1072.
[51] G. Lei, L. Zhuang, B.Y. Gan, Targeting ferroptosis as a vulnerability in cancer, Nat. Rev. Cancer 22 (2022) 381–396.
[52] J.S. Zheng, M. Conrad, The metabolic underpinnings of ferroptosis, Cell Metab. 32 (2020) 920–937.
[53] Z. Yang, S.Q. Liang, L. Zhao, H. Yang, T.M. Marti, B. Hegedüs, et al., Metabolic synthetic lethality by targeting NOP56 and mTOR in KRAS-Mutant lung cancer, Journal of experimental & clinical cancer research : CR 41 (2022) 25.
[54] Y. Gan, J. Deng, Q. Hao, Y. Huang, T. Han, J.G. Xu, et al., UTP11 deficiency suppresses cancer development via nucleolar stress and ferroptosis, Redox Biol. 62 (2023) 102705.
[55] C. Sandoval-Acuña, N. Torrealba, V. Tomkova, S.B. Jadhav, K. Blazkova, L. Merta, et al., Targeting mitochondrial iron metabolism suppresses tumor growth and metastasis by inducing mitochondrial dysfunction and mitophagy, Cancer Res. 81 (2021) 2289–2303.
[56] I. Tabas, D. Ron, Integrating the mechanisms of apoptosis induced by endoplasmic reticulum stress, Nat. Cell Biol. 13 (2011) 184–190.